Optical Engineering

OpticalEngineering.SPIEDigitalLibrary.org

Calibrating the pupil fill balance for hypernumerical aperture lithographic objective

Dawei Rui
Wei Zhang
Huaijiang Yang

SPIE.

Calibrating the pupil fill balance for hypernumerical aperture lithographic objective

Dawei Rui,[a,b,*] Wei Zhang,[a] and Huaijiang Yang[a]
[a]Changchun Institute of Optics, Fine Mechanics and Physics, Chinese Academy of Sciences, No. 3888 of Dong Nanhu Road, Jingkai District, Changchun City, Jilin Province 130033, China
[b]State Key Laboratory of Applied Optics, Changchun, Jilin 130033, China

Abstract. Projection objectives for deep-ultraviolet lithography typically have a dual-telecentric design, and the telecentricity in object space (mask) is idealized as zero. However, for combined illumination and objective lens systems, telecentricity matching on mask can result in a dramatic change in the pupil intensity distribution. Here, we propose a method of identifying the impact of the mismatch on the pupil fill and decoupling the pupil intensity balance from the telecentricity modulation. The technique is implemented in a user-defined program, and a series of simulations for a hypernumerical aperture immersion objective under off-axis illumination conditions verifies the method. [DOI: 10.1117/1.OE.54.9.095103]

Keywords: pupil fill balance; telecentricity; microlithography; optical design.

Paper 150143 received Feb. 2, 2015; accepted for publication Aug. 17, 2015; published online Sep. 21, 2015.

1 Introduction

For hyperprecision applications, deep-ultraviolet microlithography tools need to perform to a high standard in terms of both image quality and dose control. Uniform exposure is an essential target for the lithographic objective, and uniformity is typically determined through the spatial and angular distributions, or irradiance and intensity, respectively. The irradiance is attributed to the transparency consistency of the coating and materials across the entire illumination field of view (FOV), while the intensity, measured in angular space, accounts for more complex factors such as the coating inconsistency, illuminator misalignment, and mismatch between the illumination optics and projection lens.[1] These latter factors produce unbalanced pupils in different ways: coating inconsistency may only cause a symmetric radial blur in the pupil fill, while misalignment may cause axis skew and produce a tilt distribution with one side of the pupil fill being brighter than the other. Mismatch usually induces nontelecentric chief rays, hence a decentered pupil fill pattern with an asymmetric intensity distribution and a displaced mass center. Unbalanced pupil fills will degrade the contrast and even resolution of the target features on the wafer: for example, assuming a dense line and space pattern under dipole illumination with partial coherence, an unbalanced intensity that is lower along the direction perpendicular to the lines will result in a sharp exposure on one side and a blurry exposure on the other (the effects on an overlay procedure would be more severe). Thus, microlithographic systems for hyperprecision applications must have excellent balanced pupils at each FOV point and consistency within all FOV points. To this end, the pupil balance should be correctly predicted and evaluated.

There is currently no commonly accepted definition for the degree of pupil unbalance in microlithography. Here, any change in the pupil intensity by any mechanism is defined as a contribution to an unbalanced pupil; alternative definitions can be found in Refs. 2–5. However, it is important to distinguish the causes of unbalanced pupils, and in this paper, we propose a method for identifying the impact of telecentricity on the pupil fill, and distinguishing the contributions of the telecentricity from that of other factors.

The majority of projection lithographic lens in current use are dual-telecentric lenses that maximize the robustness against defocus and object displacement, such that the changes in the centroid-based distortion and reduction rate are small. In a similar way to the aerial image of the aperture stop, the pupil can be characterized by the angular distribution of the intensity, and the pupil balance can be described in terms of the uniformity of the intensity in a specific FOV in the angular plane under a certain illumination mode. However, telecentricity and the ray path coupling on the mask (owing to a combined illumination system and objective lens) can result in a dramatic deviation of up to microradians from the idealized telecentricity in the wafer plane. The tilting of the chief rays may be insignificant during aberration evaluations with a fixed focus, but when the wafer is defocused, the system is more sensitive to the reduction rate and distortion because of the tilting chief ray. Moreover, if the pupil intensity distribution in the wafer plane is measured along the optic axis direction and the practical telecentricity couples with the imaging light cone and induces a tilting of the chief ray, then the received intensity in the angular plane will be decentered. This will mean that pupil balance measurements will give results that are not accurate, thus the pupil intensity balance must be uncoupled from the telecentricity modulation.

2 Modulation of Telecentricity on Pupil Balance Detection

2.1 *Pupil Balance Criterion*

Off-axis illumination is commonly adopted to enhance both the resolution and depth of focus.[6] Figure 1 outlines

*Address all correspondence to: Dawei Rui, E-mail: davyray@163.com

0091-3286/2015/$25.00

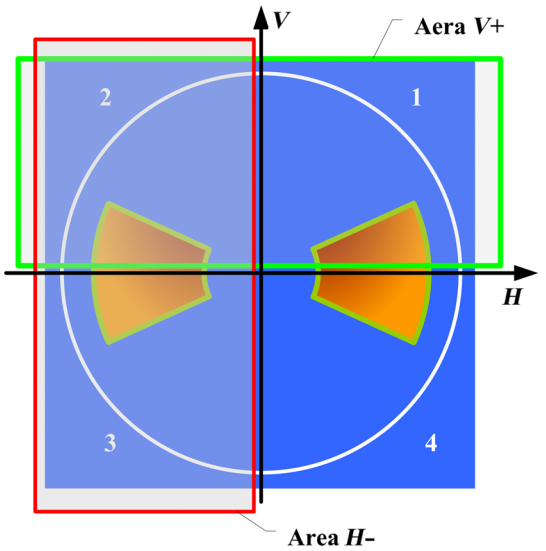

Fig. 1 Pupil division in the angular plane.

a division of the angular plane used for measuring the pupil intensity distribution under dipole illumination conditions. The plane is divided into four quadrants defined by the H and V axes such that, for example, quadrants 1 and 4 define the $H+$ area. The pupil balance can be expressed in terms of unbalanced H and V areas or unbalanced quadrants (Quad) to describe the deviation of the pupil intensity across the pupil domain.

Thus, we can define the degree of unbalance as

$$\text{Unbalance} = \frac{\max\left(\left|\int_{(i)} I - \frac{1}{n}\sum_{i=1}^{n}\int_{(i)} I\right|\right)}{\frac{1}{n}\sum_{i=1}^{n}\int_{(i)} I}, \tag{1}$$

where $\int_{(i)} I$ is the integral of the intensity over an area i, i.e., $H+$, $H-$, $V+$, and $V-$ (half-plane balance), or 1, 2, 3, and 4 (Quad balance). Typically, the degree of unbalance should be less than 4%, and lower for a hypernumerical aperture (NA) objective to ensure the smallest feature sizes are resolved.

2.2 *Telecentricity Coupling to Pupil Balance*

Figure 2 shows a ray diagram for a telecentric lithographic objective. Regardless of the diffraction effect of the reticle, if an arbitrary light cone produced by the illumination system deviates from being telecentric, then the direction of the chief ray (dashed red line) will be redefined with an angle of θ_i' with respect to the telecentric direction (dashed black line). In Fig. 2, cone $1'$ and cone $2'$ are the practical and ideal imaging cones, respectively. If the solid angle of cone $2'$ is less than the maximum clear aperture, then light in cone $1'$ will be partially blocked by the aperture stop,[7] resulting in a dramatic pupil bias in the Fourier plane. After propagating through the lens, the light is focused at Fi on the wafer. The chief-ray angle of θ_i, which is conjugate to θ_i', is introduced, and θ_i can be considered as the deviation of the practical imaging cone from the ideal imaging cone. Cone 1 will always be the practical imaging cone regardless of the angle θ_i, but in simulations with a receiver aligned in the ideal telecentric direction (e.g., cone 2), the imaging light is that in the overlapping area of cone 1 and cone 2, with part of the light in cone 1 filtered by the aperture stop. If the intensity in the practical cone is captured by, for example, a charge-coupled device camera to calculate the pupil balance, then the change in the pupil position in the pupil plane, that is, ΔH and ΔV, could be determined from θ_i. Thus, the telecentricity modifies the ray path, hence the pupil intensity distribution. The pupil balance is coupled with the telecentricity, and a similar phenomenon will occur if the lens is designed with a certain degree of object-space telecentricity rather than being ideally telecentric. In general, the pupil balance will be inaccurate unless ΔH and ΔV are corrected.

As the respective meridian and sagittal telecentricity, ΔH and ΔV can be resolved from the direction cosine (L, M, N), and (L, M, N) can be easily calculated through the built-in algorithm of Code V

$$(L, M, N) = f(L', M', N', x', y', z'), \tag{2}$$

where f is the propagation function decided by the lens parameters. (L', M', N') and (x', y', z') are the direction cosine of the chief ray on the mask and the coordinate of the conjugate FOV point on the mask, respectively. This can be implemented by Code V command interface, which can also be executed by the outer program.

2.3 *Pupil Balance Calibration on Procedure*

A pupil data matrix can be obtained from a nonsequential ray tracing simulation of the illumination. The matrix will represent the telecentricity-modulated intensity, which can then be used by a secondary program for demodulation and calibration of the pupil balance. We wrote a program [Fig. 3(a)] that combined Monte Carlo ray tracing data with sequential calculations and implemented the code within

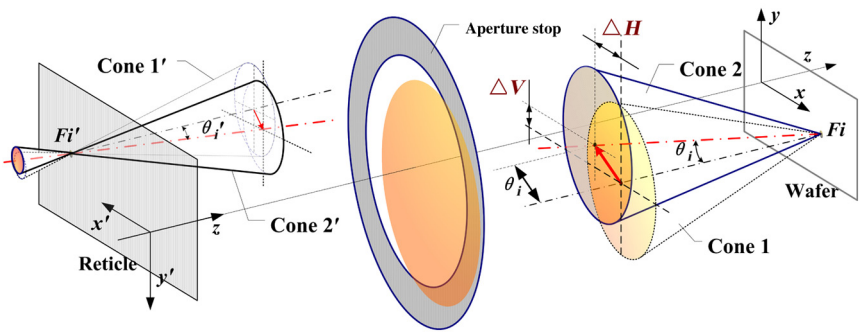

Fig. 2 Propagation of imaging light through a telecentric lithographic objective.

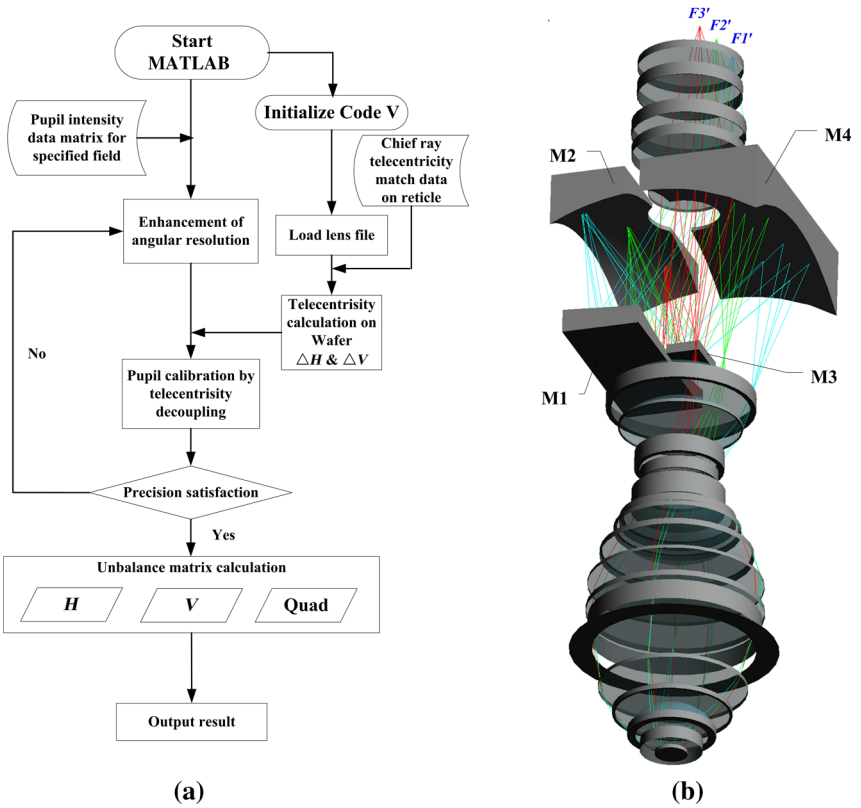

Fig. 3 Flow chart and objective: (a) program flow chart and (b) ray-tracing model of the optimized hypernumerical aperture objective.

MATLAB. Code V macros are attached to a MATLAB external procedure, and a component object model interface is used to connect the Code V with MATLAB.[8,9] The calculations are typically completed within a minute.

The calculations proceed in the following sequence:

1. The telecentricity in terms of the horizontal and vertical angular deviations (ΔH and ΔV, respectively) for a given FOV point on the wafer is calculated using Code V.
2. A stored Monte Carlo ray tracing result from the LightTools software is read automatically to provide the pupil intensity data matrix of the specific FOV point.
3. The pupil plane is divided into a grid with a finite angular resolution, and cubic spine interpolation of the intensity is implemented to enhance the angular resolution and smooth intensity fractions.
4. The nominal position of each grid point is calculated and relocated along the H and V axes until the telecentricity has been decoupled. In this step, pupil calibration is achieved, and so a demodulated intensity is obtained.
5. The result is checked against certain criteria, and steps 4 and 5 are repeated until the criteria are met.

3 Simulation Verification

A catadioptric immersion objective model (uniaxial four-mirror type: NA = 1.2) was utilized to verify the simulation. This lens was initialized from a certain structure, and optimized for high performance using Code V. The optimal wavefront errors and distortion were both below 1 nm. The absolute telecentricity values on the object and image sides were 13 mrad (about 0.74 deg) and 1.5 mrad, respectively, which were intentionally designed to investigate the effect of a telecentricity mismatch across the entire FOV. A three-dimensional view of the design model is shown in Fig. 3(b) with rays emanating from three points.

3.1 *Telecentricity at Specific FOV Point*

Both the spatial distribution of the energy and the variability in the telecentricity should be taken into account when selecting the FOV points for the simulation.

To achieve uniform illumination, most step-and-scan exposure tools employ a trapezoidal-distributed irradiance to enhance the integral energy uniformity during scanning. Figure 4(a) shows the assumed input irradiance distribution on a mask of width x and height y. The exposure FOV is 105 mm × 22 mm, and the top of the trapezoid covers ~1/3 of the exposure FOV area. The sampling points should be restricted to those within the top of the trapezoid to ensure the received energy is the same.

For catadioptric systems, in particular, a rectangular FOV will only be located in half of the clear aperture on a conjugated surface, as sketched in Fig. 4(b). Since the FOV is asymmetric, the performance along the diagonal is of interest and should be taken into consideration to investigate the total performance. The ideal region for choosing the sampling points is defined by the area common to the top of the trapezoid (dashed lines) and the diagonal line. As shown

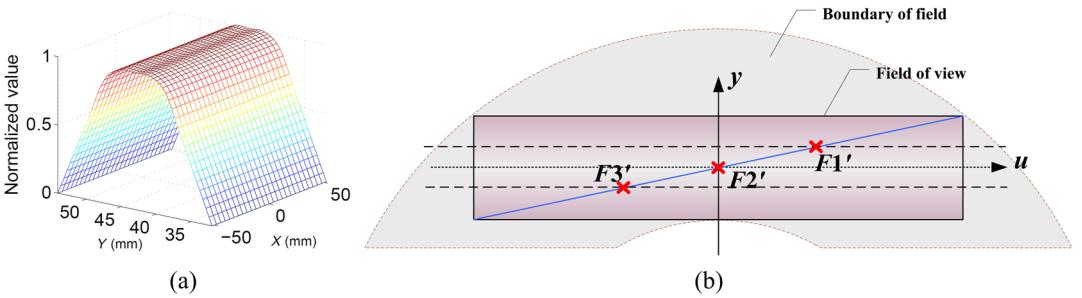

Fig. 4 Irradiance distribution and field of view (FOV) sampling: (a) trapezoidal irradiance of the object (reticle) plane and (b) FOV sampling restricted to points along the diagonal within the top of the trapezoidal area (dotted lines).

in Fig. 4(b), the points $F1'$, $F2'$, and $F3'$ and their conjugates ($F1$, $F2$, and $F3$) were chosen for the analysis. The ray paths from these points are illustrated in Fig. 3(b).

Dipole illumination was assumed for the simulations with inner and outer coherences of 0.36 and 0.71, respectively. The mask did not carry any pattern or frequency information (null mask), and the reticle feature size mainly affects the irradiance distribution on each optical surface (especially near the aperture stop) because of low-order diffraction. There are few influences on our target image.

The designed and matching values of the V component of the telecentricity on the image side are shown in Fig. 5. The asymmetry in the FOV positions is reflected in the asymmetry of the telecentricity, and the matched values are considerably different from the designed values. There is a larger amount of variation in the matched values, which vary between −0.92 and 8.57 mrad. The matching was worse at the edge of the field near $F1$, but almost perfect near $F2$ and $F3$. If the input telecentricity on the reticle is far from the designed value, then the matched telecentricity on the wafer will be different from that shown in Fig. 5, resulting in a worse performance and more difficult calculation and prediction. The matched results of ΔH and ΔV for an idealized zero-telecentricity input are listed in Table 1.

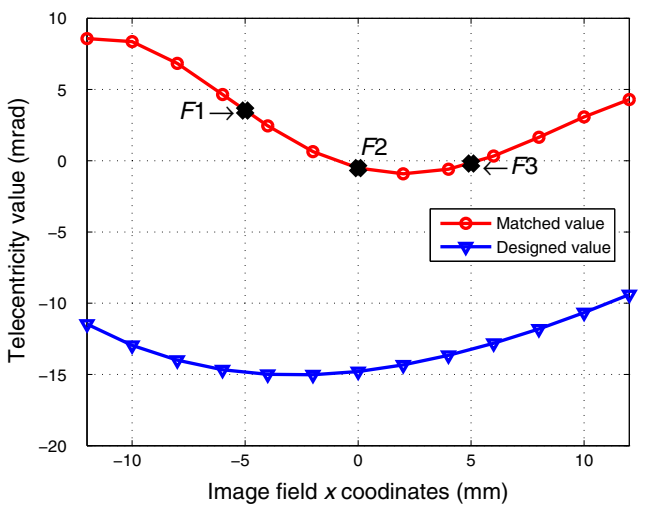

Fig. 5 Tangential component of the designed and matched telecentricity curves.

Table 1 Telecentricity on wafer with ideal zero telecentric input.

Parameters	Sampling field point on wafer		
	$F1$	$F2$	$F3$
Induced image telecentricity θ_i (mrad)	3.82	0.52	0.22
ΔH (mrad)	1.49	0	0.1
ΔV (mrad)	3.52	−0.52	−0.2

3.2 *Pupil Matrix Demodulation*

Demodulation of the pupil matrix was achieved by correcting for the detection direction on the wafer. The matrix data are based on one billion nonsequential ray tracing results, which provide a ray density sufficient enough to minimize high-frequency noise. The cubic interpolation enhanced the angular resolution to be less than 0.01 deg.

The telecentricity coupling was removed by a user-defined program, and the calibrated pupil balance in terms of H, V, and Quad were recalculated, as shown in Table 2. The histograms in Fig. 6 emphasize the effect of pupil calibration. At point $F1$, which had the largest telecentricity, the effect of calibration was the greatest for both the V and Quad balances; there was minimal telecentricity in the

Table 2 Degree of pupil unbalance with telecentricity coupled and decoupled under dipole illumination.

Field of view on wafer		Pupil unbalance		
		H (%)	V (%)	Quad (%)
$F1$	Coupled	0.27	3.75	4.09
	Decoupled	0.27	0.64	0.96
$F2$	Coupled	0.02	0.59	0.62
	Decoupled	0.02	0.04	0.07
$F3$	Coupled	0.26	0.26	0.34
	Decoupled	0.26	0.08	0.07

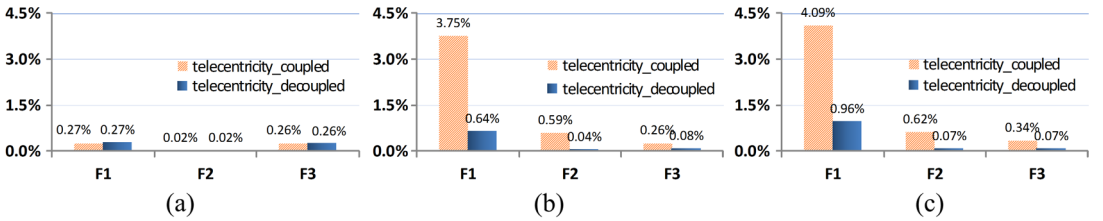

Fig. 6 Histograms of the pupil unbalance measured using the (a) H, (b) V, and (c) Quad criteria before and after calibrations.

direction parallel to the dipole, thus there was little change in the H balance.

The message we were trying to convey in Fig. 7 is the displacement of pupil fill energy distribution between coupled and decoupled pupil fill. The legend for "coupled" data is hollow-mesh type and the legend for "decoupled" data is filled-surface type. In each single plot with the same angular coordinate system, the decoupled and coupled pupil patterns are plotted together, and the decoupled pupil data matrix has a tiny spatial shift relative to its original position (coupled data). As can be seen from Figs. 7(c) and 8, there is a larger deviation along the V direction at $F1$ than the other two FOV points, which is consistent with the result in Table 2.

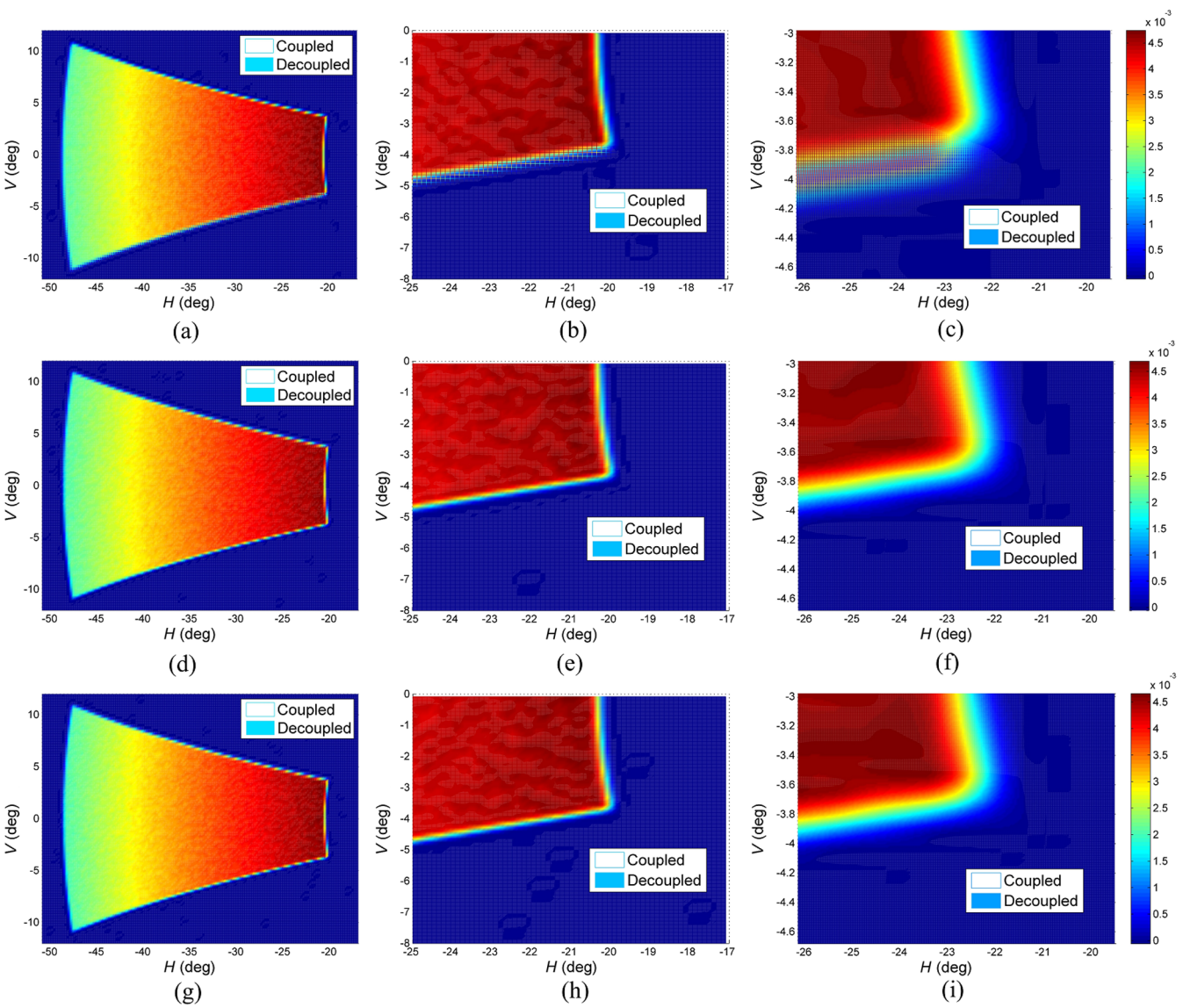

Fig. 7 Comparison of coupled (mesh) and decoupled (filled) pupil fills: (a), (b), and (c) local pupil fill at $F1$; (d), (e), and (f) local pupil fill at $F2$; (g), (h), and (i) local pupil fill at $F3$. Local features are shown for (a), (d), and (g) 1/20; (b), (e), and (h) 1/250; and (c), (f), and (i) 1/1250 of the total area.

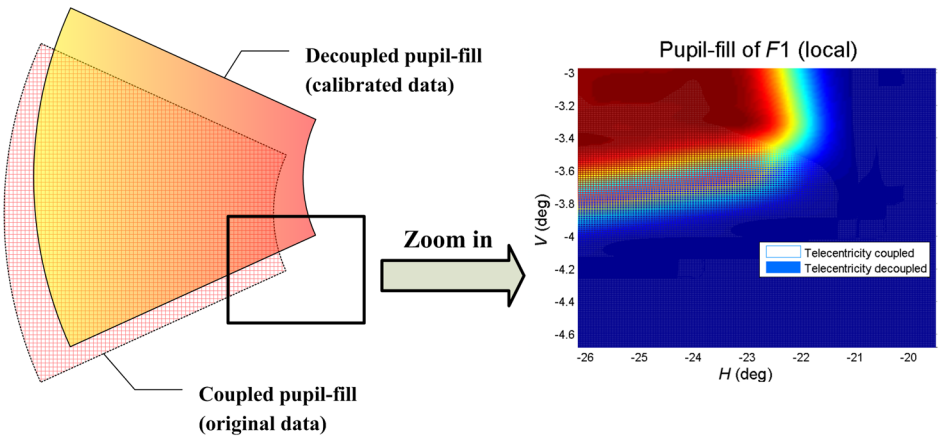

Fig. 8 Illustration of pupil fill displacement.

4 Conclusion

We have proposed a method of calibrating the pupil balance based on a user-defined program that removes the effects of the practical telecentricity. The program was demonstrated to be functional and efficient in calibrating and calculating the pupil fill through a simulation with an optimized immersion lithographic lens. The technique has benefits for not only prediction veracity during simulations, but also performance measurements during system tests. The real coupling level of the telecentricity in the pupil balance as well as the intrinsic behavior of the objective can be obtained. Future work will focus on combining this method with test facilities for measuring the performance of lithographic lenses.

Acknowledgments

This research was supported by the Chinese National Key Scientific and Technological Project-02 (No. 2009ZX02205).

References

1. J. J. Biafore et al., "The causes of horizontal–vertical (H–V) bias in optical lithography: dipole source errors," *Proc. SPIE* **6520**, 65203V (2007).
2. S. P. Penwick, "Quasi-telecentricity: the effects of unbalanced multipole illumination," *Proc. SPIE* **6520**, 65202W (2007).
3. H. Bai and S. P. Sadoulet, "Large-format telecentric lens," *Proc. SPIE* **6667**, 666705 (2007).
4. J. Shin et al., "Measurement technique of nontelecentricity of pupil-fill and its application to 60 nm NAND flash memory patterns," *Proc. SPIE* **5754**, 294–302 (2005).
5. G. McIntyre et al., "Modeling and experiments of non-telecentric thick mask effects for EUV lithography," *Proc. SPIE* **7271**, 72711C (2009).
6. R. Voelkel et al., "Advanced mask aligner lithography: new illumination system," *Opt. Express* **18**, 20968–20978 (2010).
7. W. J. Smith, *Modern Optical Engineering*, pp. 175–204, McGraw-Hill, California (2008).
8. W. Xu et al., "Automatic clocking optimization for compensating two-dimensional tolerances," *Opt. Express* **21**, 22145–22152 (2013).
9. C. Liu et al., "Wavefront aberration compensation of projection lens using clocking lens elements," *Appl. Opt.* **52**, 5398–5401 (2013).

Dawei Rui received a Master's Degree from UESTC in 2012. He served as a product engineer of optical communication in OPLINK Ltd. from 2007 to 2008. Currently, he is a research associate of the Changchun Institute of Optics, Fine Mechanics and Physics, Chinese Academy of Sciences (CIOMP) with research interests in optical system design, especially for lithographic objectives, interferometers, and projection display systems. His awards include one authorized National Patent and five academic papers.

Wei Zhang received his PhD degree from the Department of Physics, University of Science and Technology of China in 2007. Currently, he is an associate professor of the CIOMP. His research interests are collaborative design of optomechanical systems, computer-aided alignment, and diffraction optics.

Huaijiang Yang received his PhD from Beijing Institute of Technology in 1996. Currently, he is the chief expert and chairman of the Engineering Research Center of Extreme Precision Optics in CIOMP. His research interests mainly include subnano-optical fabrication and metrology over full-band spatial frequency, multispectral imaging detection and fusion, and nanodrive control and its application.